PCCP

Cite this: *Phys. Chem. Chem. Phys.*, 2011, **13**, 6849–6857

www.rsc.org/pccp

PAPER

An *in situ* STM/AFM and impedance spectroscopy study of the extremely pure 1-butyl-1-methylpyrrolidinium tris(pentafluoroethyl)trifluorophosphate/Au(111) interface: potential dependent solvation layers and the herringbone reconstruction

Rob Atkin,†[a] Natalia Borisenko,†[bc] Marcel Drüschler,†[d] Sherif Zein El Abedin,†[bce] Frank Endres,†*[bc] Robert Hayes,†[a] Benedikt Huber†[d] and Bernhard Roling†[d]

Received 10th December 2010, Accepted 17th February 2011
DOI: 10.1039/c0cp02846k

The structure and dynamics of the interfacial layers between the extremely pure air- and water-stable ionic liquid 1-butyl-1-methylpyrrolidinium tris(pentafluoroethyl)trifluorophosphate and Au(111) has been investigated using *in situ* scanning tunneling microscopy, cyclic voltammetry, electrochemical impedance spectroscopy, and atomic force microscopy measurements. The *in situ* scanning tunnelling microscopy measurements reveal that the Au(111) surface undergoes a reconstruction, and at −1.2 V *versus* Pt quasi-reference the famous ($22 \times \sqrt{3}$) herringbone superstructure is probed. Atomic force microscopy measurements show that multiple ion pair layers are present at the ionic liquid/Au interface which are dependent on the electrode potential. Upon applying cathodic electrode potentials, stronger ionic liquid near surface structure is detected: both the number of near surface layers and the force required to rupture these layers increases. The electrochemical impedance spectroscopy results reveal that three distinct processes take place at the interface. The fastest process is capacitive in its low-frequency limit and is identified with electrochemical double layer formation. The differential electrochemical double layer capacitance exhibits a local maximum at −0.2 V *versus* Pt quasi-reference, which is most likely caused by changes in the orientation of cations in the innermost layer. In the potential range between −0.84 V and −1.04 V, a second capacitive process is observed which is slower than electrochemical double layer formation. This process seems to be related to the herringbone reconstruction. In the frequency range below 1 Hz, the onset of an ultraslow faradaic process is found. This process becomes faster when the electrode potential is shifted to more negative potentials.

Introduction

In recent years, ionic liquids (ILs) have attracted considerable research interest in the fields of surface science and physical chemistry. Wide electrochemical and thermal windows, good ionic conductivities, acceptable viscosities, extremely low vapor pressures and the ability to solubilize many chemical species make ILs interesting solvents for electrochemical applications. In Clausthal we found that even small variations in the cation/anion combination can drastically influence electrochemical processes. For example, by variation of just the cation either nanocrystalline or microcrystalline Al is electrodeposited.[1] Since the Al species present in the bulk of both ILs are virtually identical,[2] it seems likely that the near surface layers at the electrodes differ for both ILs:[3] Si_xGe_{1-x} deposits, for example, made potentiostatically from an equimolar solution (0.1 mol L^{-1}) of $SiCl_4$ and $GeCl_4$ in 1-ethyl-3-methylimidazolium bis(trifluoromethylsulfonyl)amide, [EMIm]TFSA, have a lower Si content than those obtained from 1-butyl-1-methylpyrrolidinium bis(trifluoromethylsulfonyl)amide, $[Py_{1,4}]$TFSA, under the same conditions;[4] the particle composition and size are influenced by the IL, and the overall deposition rate varies due to differences in the diffusion coefficients of $SiCl_4$ and $GeCl_4$ in each IL. Thus, the kinetics of metal and semiconductor deposition seem to depend on the structure and the dynamics of the interfacial layers between the IL and the metal surface.

[a] *Centre for Organic Electronics, Chemistry Building, The University of Newcastle, Callaghan, New South Wales, 2308, Australia. E-mail: Rob.Atkin@newcastle.edu.au*
[b] *Institute of Particle Technology, Clausthal University of Technology, Arnold-Sommerfeld-Strasse 6, 38678 Clausthal-Zellerfeld, Germany. E-mail: frank.endres@tu-clausthal.de*
[c] *EFZN Goslar, Am Stollen 19, 38640 Goslar, Germany*
[d] *Department of Chemistry, University of Marburg, Hans-Meerwein-Strasse, 35032, Marburg, Germany. E-mail: roling@staff.uni-marburg.de*
[e] *Electrochemistry and Corrosion Laboratory, National Research Centre, Dokki, Cairo, Egypt*
† The authors are listed in alphabetic order and have all equally contributed to this paper.

The interface of a classical diluted electrolyte solution with a metal electrode is commonly described by mean-field models: the Helmholtz model, the Gouy–Chapman model and the Stern model. However, these models were developed for diluted electrolyte solutions and therefore are not applicable for the description of ILs due to the high number density of mobile ions. In mean-field models, the interactions of a solvated ion with a charged electrode and with other ions in the interfacial (innermost) layer are described by a mean electric potential. In contrast, an IL represents a dense system of cations and anions with no solvent, so the individual interactions between neighbouring ions should play an important role.[5–7] Only the finite volume occupied by the ions, which sets the upper limit for the ion concentration at the electrode interface, can be taken into account at the mean-field level.[8–10]

The solid/IL interface is more complex than that of molecular solvents, and can be divided into three distinct zones: the interfacial (innermost) layer, which refers to ions in direct contact with the solid surface and is the most spatially organized; the bulk phase, which refers to the bulk liquid region that may be structured or unstructured depending on the degree of ion amphiphilicity[11] and the transition zone, which refers to the region over which the more pronounced interfacial (innermost) layer structure decays to the bulk morphology. Atomic Force Microscopy (AFM) has been used to probe IL structure in the interfacial (innermost) layer and transition zone adjacent to a wide variety of substrates.[12–16] It was found that the transition zone in both protic and aprotic ILs is characterized by 2–5 ion pair layers. The push-through forces for these layers increase closer to the surface suggesting that ordering is more pronounced close to the interface. X-Ray reflectivity studies have revealed similar findings for ILs with the tris(pentafluoroethyl)trifluorophosphate (FAP^-) anion,[17] which is employed for the present study. The surface interaction of [EMIm]TFSA and [$Py_{1,4}$]TFSA with Au(111) has also been investigated using AFM and *in situ* scanning tunnelling microscopy (STM) measurements.[15] AFM showed that 3–5 ion pair layers were present for [EMIm]TFSA and [$Py_{1,4}$]TFSA, but [$Py_{1,4}$]TFSA was 4 times more strongly adsorbed on the Au(111) surface than [EMIm]TSFA at open circuit potential (ocp). *In situ* STM measurements revealed that the adsorption of the ILs leads to a restructuring of the Au surface and this adsorption seems to be dependent on the electrode potential. These results are in accordance with sum frequency generation (SFG) measurements,[18–20] which concluded that a change in the electrode potential will result in a variation of ion orientation in the interfacial (innermost) layer.

In recent years the potential-dependent capacitance of the interfacial layers at metallic electrodes has been studied for a range of ILs.[21–34] However, most capacitance measurements were carried out in a relatively narrow frequency range and a systematic analysis of the influence of impurities on the measured capacitance values was not performed. In some publications the IL quality is not reported, and the results are in part contradictory. In our opinion the conflicting data are likely a consequence of impurities for example halides and water. Hysteresis effects in the potential dependence of the electrochemical double layer (EDL) capacitance have been reported in ref. 26. Quite recently, the Marburg group has shown that the potential-dependent EDL capacitance of [EMIm]TFSA and [$Py_{1,4}$]TFSA at a polycrystalline Pt electrode is characterized by hysteresis effects, which are most likely related to slow pseudocapacitive processes at frequencies below 10 Hz.[29] The combination of capacitance measurements with *in situ* STM and AFM methods can clarify the nature of these pseudocapacitive processes.

ILs can exhibit strong liquid- and potential-dependent layering on solid electrodes which might hinder atomic-resolution STM imaging of single crystalline electrodes. It has been reported that Au(100) can be probed quasi-atomically with AFM,[35] however, no information on the purity of the IL investigated is provided. Furthermore, ILs with the BF_4^- anion (most likely with Cl^- impurities) show a potential-dependent adsorption on the Au(100) surface and in a certain potential regime the adsorption of the anion layer can be probed quasi-atomically with *in situ* STM.[36]

In the present paper, the structure and dynamics of the interfacial layers between the air- and water-stable IL 1-butyl-1-methylpyrrolidinium tris(pentafluoroethyl)trifluorophosphate ([$Py_{1,4}$]FAP) and Au(111) has been investigated using STM, cyclic voltammetry (CV), electrochemical impedance spectroscopy (EIS), and AFM measurements. *In situ* STM measurements reveal that the Au(111) surface undergoes a reconstruction, and at −1.2 V (*vs.* Pt quasi-reference) the ($22 \times \sqrt{3}$) "herringbone" superstructure is probed. AFM force–distance profiles show that the IL becomes more structured at higher cathodic potentials, with both the number of detectable layers and push-through forces increasing. The EIS measurements reveal a capacitive process at the IL/Au(111) interface which is considerably slower than EDL formation. This slow capacitive process can only be detected in a potential range from −0.84 V to −1.04 V and seems to be related to the herringbone reconstruction.

Experimental

[$Py_{1,4}$]FAP was purchased from MERCK in highest available quality. The liquid was custom-made and the purity protocol delivered by Merck showed that all detectable impurities were below 10 ppm. HF and oxide levels were below the detection limit of 10 ppm. It is important to mention that impurities in ILs, which are observed too often in commercial ILs (even in apparently ultrapure quality), can strongly alter the surface processes leading to misinterpretations.[37] If the liquid is synthesized for example by a metathesis reaction from a metal salt and an organic halide, organic impurities (decomposition products of anions and/or cations, side products) and Li^+, Na^+, K^+ and halides can be found in the 1000 ppm range even in apparently ultrapure ILs. Furthermore, purification procedures may introduce SiO_2 or Al_2O_3 particles, which can accumulate at the interface and influence bulk or interfacial properties. Prior to use all ILs were analyzed using CV, XPS and *in situ* STM to ensure the purity. Furthermore, for fundamental studies custom-made ILs of the highest possible purity are required to avoid misinterpretation. Additionally, the IL was dried under vacuum (10^{-3} mbar) at 100 °C to H_2O contents well below 1 ppm and stored in a closed bottle in a desiccator (at Newcastle), in an Ar-filled glove box with H_2O and O_2 contents of below 2 ppm (OMNI-LAB from Vacuum-Atmospheres)

(in Clausthal) and in a N_2-filled glove box with H_2O and O_2 contents of below 1 ppm (LABstar from MBRAUN GmbH) (in Marburg). *In situ* STM, AFM and EIS measurements were carried out using samples of the same IL which were sent in sealed ampoules to the partners. The substrates for AFM and STM experiments and the working electrode (WE) were Au(111) (a 300 nm thick film on mica) purchased from Agilent. Directly before use, the substrates were carefully heated in a H_2-flame to minimize possible surface contaminations. CV measurements were carried out in the glove box using a Parstat 2263 potentiostat/galvanostat (Princeton Applied Research) controlled by a PowerCV software. The electrochemical cell was made of polytetrafluoroethylene (Teflon) and clamped over a Teflon-covered Viton O-ring onto the substrate, thus yielding a geometric surface area of the WE of 0.3 cm^2. Pt wires (Alfa Aesar, 99.99%) of 0.5 mm diameter were applied as quasi-reference (RE) and counter (CE) electrodes, respectively. From our experience, Pt has a sufficiently stable electrode potential under *in situ* STM conditions. Directly before use the Pt wires were cleaned for 15 min in an ultrasonic bath in acetone followed by heating in a H_2-flame to red glow for a few minutes to minimize surface contaminations.

For the EIS measurements, the Marburg group used a home-made cell with a sample volume of 150 μL. During the measurements, the temperature was kept at 30 ± 0.1 °C by means of a Eurotherm 2416 temperature controller. A three-electrode configuration was used with a polycrystalline Pt wire acting as RE, a Pt crucible acting as CE (80% Pt, 20% Rh, purchased from Mettler Toledo GmbH), and a Au single crystal (Au(111), MaTeck GmbH) acting as WE. The Au single crystal exhibits a cylindrical shape with a diameter of 3 mm and a height of 5 mm. The Au(111) surface was orientated to values better than 1°. To allow for an easier connection to the cell, a Au wire was soldered to the rear part of the cylinder. Before any measurement, the single crystal was annealed in a propane-gas flame to light red heat for 30 s, and then was allowed to cool under Ar flow (see also ref. 38 and 39). It has been shown by means of STM that surfaces prepared in this way show broad atomically flat terraces which are well-ordered.[40] The contact between the Au(111) surface and the IL was established by the dipping technique:[41] The polished and orientated surface of the single crystal was moved in the direction of the IL, until it was in contact with its surface. When the electrode surface was slowly moved backwards, a thin tube of the IL was formed, since the IL adhered to the electrode surface. By using this technique, a contact between the non-orientated and non-polished side walls of the single crystal and the IL could be avoided. The potential of a Pt RE is assumed to be determined by the formation of an oxide film on the Pt surface.[42] In order to prepare an oxide layer in a reproducible fashion, the Pt wire was annealed in a propane-gas flame for a few minutes. In this way, the potential shift of the RE during measurements over extended time intervals could be limited to less than 100 mV, as compared to values of several 100 mV reported in the literature.[43] The electrochemical cell was connected to a Novocontrol modular measurement system consisting of an Alpha-AK high resolution impedance analyser and a POT/GAL 15V/10A electrochemical interface. Using a freshly annealed Au single crystal electrode, impedance measurements were carried out with different dc potentials applied to the WE superimposed by a rms ac voltage of 10 mV. Impedance spectra were collected in a frequency range from 10 mHz to 1 MHz. Before the start of an impedance measurement, the system was allowed to equilibrate over a period of 10 min. The impedance spectra were fit using the WinFit software (Novocontrol Technologies).

AFM force measurements were acquired continuously using a Digital Instruments NanoScope IIIa Multimode AFM in contact mode in an incubator at 21 °C. The scan rate and scan size were kept between 0.1 and 0.5 Hz and 10 and 50 nm, respectively. One standard sharpened tip Si_3N_4 cantilever (Digital Instruments, CA) was used for all measurements. The spring constant was measured to be 0.07 N m^{-1} ± 0.005 (thermal noise method).[44] The tip was carefully rinsed in Milli-Q H_2O and irradiated with ultraviolet light for 40 min prior to use. The IL was held in an AFM fluid cell, sealed using a silicone O-ring. Both of these were cleaned by sonication for 30 min, rinsed copiously in distilled ethanol and Milli-Q H_2O, and then dried using filtered N_2. A modified AFM cell setup was used to acquire force curves as a function of potential. The changes made were inspired by a design proposed by Wanless *et al.*[45] A thin cylindrical strip of Cu metal and 0.25 mm Pt wire were used as the CE and RE, respectively. The CE and RE were cleaned firstly in diluted HCl acid solution and then washed with distilled ethanol and Milli-Q H_2O and dried using filtered N_2. The CE was mounted with the O-ring in the groove of the fluid cell. This was to ensure that the effective area of the CE is relatively large and axially symmetric with respect to the WE and to establish an equipotential WE surface. The RE was located directly above the centre of the WE surface by securing the Pt wire through the outlet valve of the fluid cell. This configuration enabled the RE to be positioned as close as possible to the WE (minimizing ohmic losses) and thus enable the potential difference between the two electrodes to be readily controlled. The electrodes were connected to an EG & G Princeton Applied Research Model 362 Scanning Potentiostat.

The features of the AFM force curves at a given surface potential did not alter over a 48 h period. Typical start distances for force scans were 30–50 nm from the Au(111) surface. The maximum applied force in contact was between 30 and 500 nN. However, no evidence for structure was detected at forces greater than 30 nN in any system. Repeat experiments revealed that the number and period of the steps was constant. Every surface potential was studied over three or more separate experiments.

STM experiments were performed at 23 °C using in-house-built STM heads and scanners under inert gas conditions (H_2O and O_2 < 2 ppm) with a Molecular Imaging PicoScan 2500 STM controller in feedback mode. Assembling of the STM head and filling of the electrochemical cell were performed in an Ar-filled glove box solely reserved for assembling of STM heads. The STM head was placed inside an Ar-filled vacuum-tight stainless steel vessel, to ensure inert gas atmosphere during the STM experiments, transferred to the air-conditioned laboratory (T = 23 ± 1 °C) and placed onto a vibration damped table from IDE (Germany). STM tips were made by electrochemical etching of Pt–Ir wires (90/10, 0.25 mm diameter) with a 4 mol L^{-1} NaCN solution and subsequently electrophoretically coated with an electropaint (BASF ZQ 84-3225 0201). During the STM experiments the potential of the WE was controlled by the PicoStat from Molecular Imaging/Agilent.

Results and discussion

Cyclic voltammetry

Fig. 1 represents a typical cyclic voltammogram of the custom-made $[Py_{1,4}]FAP$ IL on Au(111) at 25 °C. Scans were initially swept cathodically from the open circuit potential (ocp) (−0.2 V) with a scan rate of 10 mV s^{-1}. This is the potential regime in which the EIS, STM and AFM measurements were performed, and we concentrate on the cathodic regime for this paper. $[Py_{1,4}]FAP$ IL exhibits an electrochemical window of about 5.9 V (inset in Fig. 1) limited by Au oxidation and the irreversible reduction of the organic cation. The broad oxidation process from 0 V to +1.5 V (inset) is correlated with the oxidation of the reduction product of the cation as this process does not appear if the scan is reversed at −3.0 V. While this cyclic voltammogram looks more or less perfect, zooming in the potential range between −3.0 V and +1.0 V at least 4 cathodic processes (C_1–C_4) can be identified (Fig. 1). The C_1–C_3 cathodic waves are likely correlated with different surface processes that occur upon IL adsorption. *In situ* STM reveals the formation of the herringbone superstructure in the regime of C_1 and C_2. In the regime of C_3 the herringbone structure disappears. The AFM results described below indicate that strong cation adsorption occurs. The broad process C_4, which occurs prior to the decomposition of $[Py_{1,4}]^+$, is possibly correlated with the partial reduction of the organic cation. The oxidation peaks A_2 and A_3 are directly correlated with the cathodic processes C_2 and C_3 as these anodic waves appear once the scanning reaches potentials that are required for C_2 and C_3.

Electrochemical impedance spectroscopy

In the present study, the EIS measurements were carried out at selected WE dc potentials ranging from +0.2 V to −2.0 V *vs.* Pt RE. The dc potentials were superimposed by a rms ac voltage of 10 mV with varying frequency in the range from 10 mHz to 1 MHz. For any frequency, the amplitude of the voltage U_0, the amplitude of the current $I_0(\nu)$ and the phase shift between voltage and current, $\varphi(\nu)$, were used to calculate the complex impedance,

$$\hat{Z}(\nu) = \frac{U_0}{I_0(\nu)} \cdot \exp(-j\varphi(\nu)).$$

Often, frequency-dependent complex impedance data $\hat{Z}(\nu)$ are plotted in a Nyquist representation, *i.e.*, the imaginary part $Z''(\nu)$ is plotted *versus* the real part $Z'(\nu)$.[46,47] Fig. 2 shows an exemplary Nyquist plot for the system $[Py_{1,4}]FAP$/Au(111) at a WE potential of −0.2 V. In this representation, ideal capacitive behavior

$$\hat{Z}(\nu) = \frac{1}{j2\pi\nu \cdot C}$$

would manifest in a line parallel to the $Z''(\nu)$ axis. While the data in Fig. 2 clearly reveal deviations from an ideal capacitive behavior, the Nyquist representation is not well-suited for resolving different capacitive processes. Better suited is a plot of the data in the complex capacitance plane as shown for different dc potentials in Fig. 3a and b. The complex capacitance $\hat{C}(\nu)$ is calculated from the complex impedance $\hat{Z}(\nu)$ *via* $\hat{C}(\nu) = 1/(j2\pi\nu \cdot \hat{Z}(\nu))$.[46] The real part $C'(\nu)$ represents the stored electrical energy, while the imaginary part $C''(\nu)$ represents the dissipated energy. At all dc potentials, a slightly suppressed high-frequency semicircle due to EDL formation is detected. This semicircle starts at the bulk capacitance C_{bulk} and would intersect with the $C'(\nu)$ axis at the double layer capacitance C_{EDL}, if there were no additional capacitive processes at the interface. However, the data in Fig. 3a and b clearly reveal the existence of such additional processes. At potentials more positive than −0.5 V, the onset of an ultraslow process is detected, see Fig. 3a. When the potential becomes more negative than −0.5 V, this process becomes faster and shows almost faradaic behavior (phase angle almost 0°) in the limit of low frequencies, see Fig. 3b. The nature of this process is unclear at present.

The most remarkable EIS result is the existence of a second capacitive process in a potential range from −0.84 V to −1.04 V, showing up as a second semicircle in the capacitance plane, see Fig. 3b. This process is considerably slower than EDL

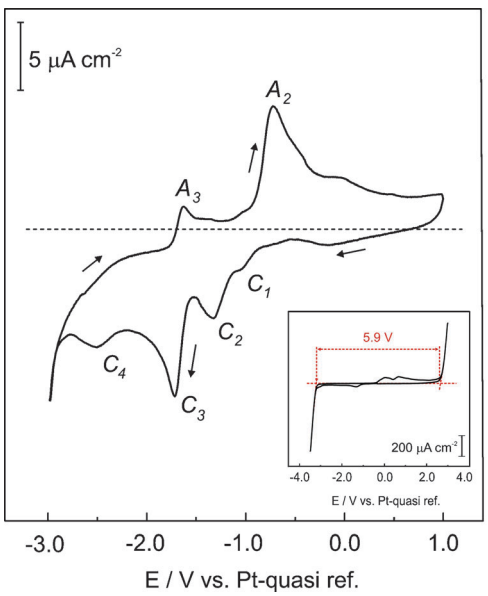

Fig. 1 Cyclic voltammogram of $[Py_{1,4}]FAP$ on Au(111) at 25 °C at a scan rate of 10 mV s^{-1}.

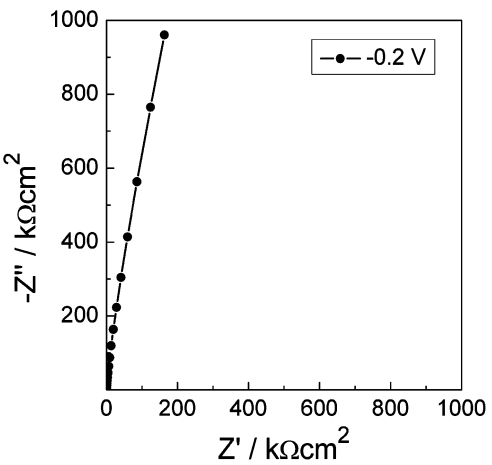

Fig. 2 Nyquist plot for the $[Py_{1,4}]FAP$/Au(111) interface at a dc-potential of −0.2 V and at 30 °C.

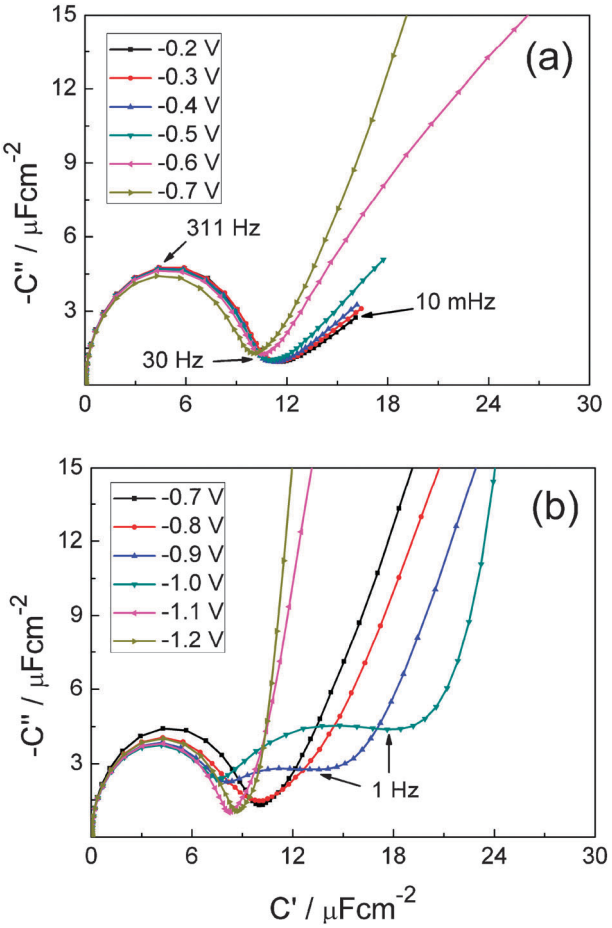

Fig. 3 Plot of the complex capacitance plane for the $[Py_{1,4}]FAP$/Au(111) interface at different dc potentials and at 30 °C. The semicircle at frequencies above 30 Hz is attributed to EDL formation.

formation, but its capacitance relaxation strength is similar to the EDL capacitance. The STM results indicate that in this potential range, the major part of the herringbone reconstruction takes place. At −1.2 V, the reconstruction seems to be completed. Therefore, we suggest that the slow capacitive process reflects charge flow to the Au(111) caused by the reconstruction process.

For a quantitative analysis, complex impedance data are often fitted to equivalent circuits. In the present study, we use a different approach. Since we are mainly interested in the capacitance relaxation strengths of different processes at the $[Py_{1,4}]FAP$/Au(111) interface, we use an empirical Cole–Cole type expression[48] to fit the slightly suppressed semicircles in the complex capacitance plane (Fig. 3):

$$(\hat{C}(\nu) - C_\infty) = \sum_{i=1}^{n} \frac{\Delta C_i}{1 + (j2\pi\nu\tau_i)^{\alpha_i}} \qquad (1)$$

Here, C_∞ is the bulk capacitance of the IL, while ΔC_i and τ_i denote the capacitance relaxation strength and the relaxation time of process i, respectively. This kind of approach is well known from the analysis of dielectric relaxation processes in supercooled liquids and polymers.[48] As an example, Fig. 4 shows the complex capacitance plane at a potential of −0.96 V together with a fit to eqn (1). The capacitance relaxation strength of the fastest process $n = 1$, ΔC_1, is identified with the EDL capacitance C_{EDL}. Note that the capacitance relaxation strength ΔC_1 should not be confused with the C_1 peak in the CV. In Fig. 5, C_{EDL} is plotted *versus* the electrode potential. A broad peak in C_{EDL} is detected around −0.4 to −0.2 V. This feature may be caused by changes in the orientation of cations in the innermost layer, as suggested by the AFM results discussed later. At −1.0 V, there is a local minimum of the capacitance followed by a slight increase towards more negative potentials. Thus, even up to highly negative electrode potentials of −2.0 V, positive counter charge can be accumulated closely to the Au(111) surface. We do not find evidence for lattice saturation effects at highly negative potentials as predicted by Kornyshev's theory.[10]

As already mentioned, the slow capacitive process is only detectable in a potential window from −0.84 V to −1.04 V. As seen from Fig. 6, the capacitance relaxation strength of this process increases when shifting the electrode potential to more negative values.

AFM measurements

The atomically smooth Au(111) surfaces employed here are ideal substrates for this type of AFM investigation, as low roughness enhances the near surface structure.[12,16] This means that the changes in force profiles that occur with potential may be directly correlated with variation in IL near the surface structure.

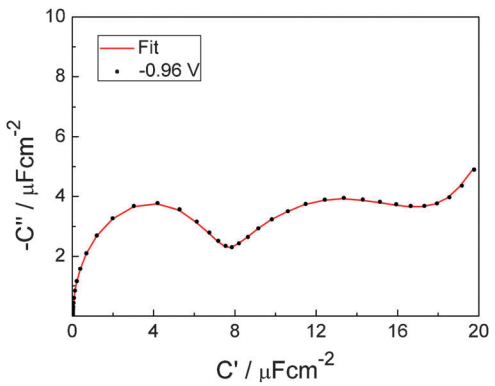

Fig. 4 Complex capacitance data for the $[Py_{1,4}]FAP$/Au(111) interface at −0.96 V and 30 °C (black points) and fit to eqn. (1) with $n = 3$ (red line)

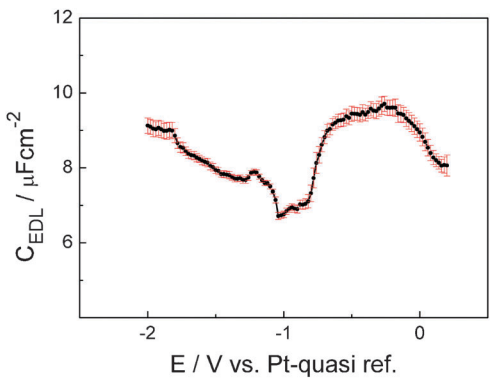

Fig. 5 EDL capacitance C_{EDL} *versus* electrode potential for the $[Py_{1,4}]FAP$/Au(111) interface at 30 °C.

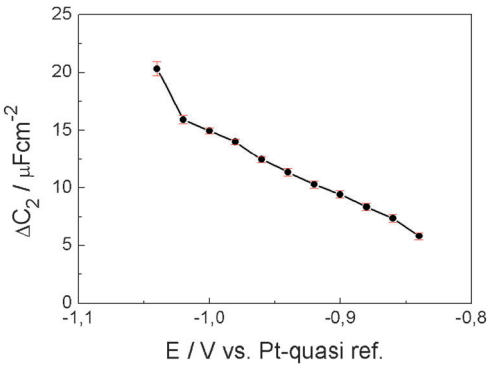

Fig. 6 Capacitance relaxation strength of the slow capacitive process at the [$Py_{1,4}$]FAP/Au(111) interface *versus* electrode potential.

Fig. 7a shows force-separation profiles for an AFM tip approaching the Au(111) surface at ocp in [$Py_{1,4}$]FAP. The form of the data resembles previous AFM measurements at the ocp with similar ILs on Au(111) and can be explained as follows. Beyond ~6 nm, zero force is recorded as the tip experiences negligible resistance moving through the IL towards the Au(111). This is significant, as it shows that the AFM is insensitive to any structure that might exist in the bulk liquid. At ~4.0 nm the tip encounters the first outermost detectable layer and pushes against it. The force increases up to 1.1 nN then the tip ruptures the layer and 'jumps' 0.9 nm before encountering another layer 3.1 nm from the interface, and the process is repeated. Four 0.9 nm sized steps in the data are detected, in excellent agreement with the diameter of the [$Py_{1,4}$]FAP ion pair (of 0.89 nm) determined from the measured bulk density. The absence of data points between 4 and 5 nm in the profile suggest a fifth, weak layer may be present. The magnitude of the push-through force for each layer increases as the tip moves closer to the surface. This indicates that IL structure is more pronounced closer to the Au(111) surface.

The width of the step closest to the surface is 0.35 nm, which is 60% smaller than subsequent steps, which were 0.9 nm in accordance with the calculated ion pair dimension. While AFM cannot determine the composition of the innermost layer unambiguously, the dramatic reduction in step width must mean that either the relative number of cations and anions, and/or their average orientations, is substantially different in the innermost layer. SPARTAN calculations suggest that the length of the cation is (0.37 ± 0.2) nm along shorter axis while the FAP anion is (0.57 ± 0.2) nm, consistent with the values reported by Mezger *et al.*[17] Based on these values it seems likely that the innermost layer is at least somewhat enriched in the cation; SFG experiments have shown that cations adsorbed to electrode surfaces have their alkyl chains tilted relative to surface normal,[19,20] which will further reduce the interfacial layer thickness. Even at low positive or neutral metal polarizations, the innermost layer has been shown to be composed of cations specifically adsorbed *via* their neutral alkyl chains.[36–38] As the innermost layer width is less than anion dimension by ~35%, the anion must either be excluded from the layer entirely (which seems unlikely on electrostatic grounds), present in a concentration sufficiently low such that it does not effect the measured AFM step size within resolution, or present at high concentrations but incorporated into the adsorbed cation palisade layer

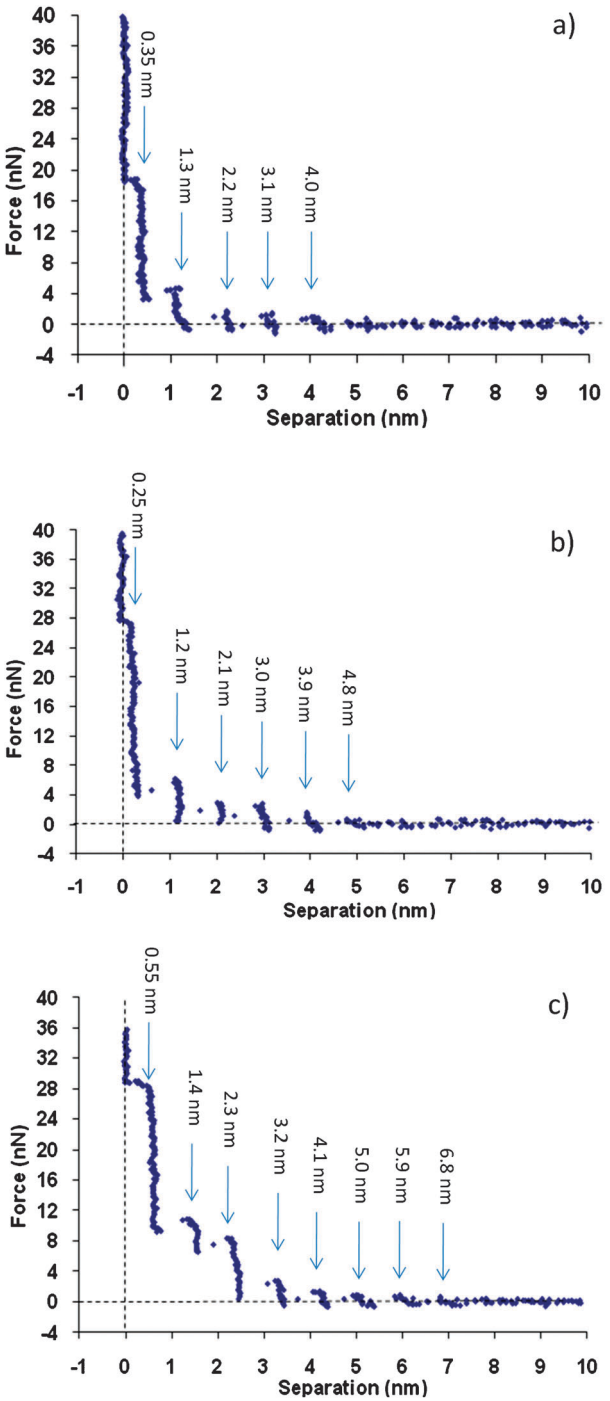

Fig. 7 Typical force *versus* distance profiles for an AFM tip approaching from a Au(111) surface in [$Py_{1,4}$]FAP at (a) ocp (b) −1.0 V (*vs.* Pt) (c) −2.0 V (*vs.* Pt).

in an orientation that is relatively compressed. It is our opinion that the true situation is some combination of the latter two possibilities.

In isolation, AFM force measurements are unable to elucidate ion orientation within this layered morphology. Whilst the bulk structure has not been reported for this IL, similar aprotic ILs[49] possess bulk structure due to segregation of charged and uncharged molecular groups. This results in the formation of well-defined polar and apolar domains. At the Au(111) surface, this

arrangement of polar and apolar layers will be retained, as the interionic forces that lead to bulk structure are also expressed at interfaces.[16] In fact, the interaction between ILs and solid surfaces has an organizing effect, such that the structure close to the interface is more pronounced than the bulk morphology. At ocp, the negative surface charge will produce an interfacial (innermost) layer enriched in the cation. The order associated with this innermost layer decays to the bulk morphology over ~5 nm.

When a potential bias of −1.0 V or −2.0 V is applied to the Au(111) surface (Fig. 7b and c respectively), three key changes are detected in the force profile. Firstly, individual ion pair steps appear sharper and better defined, and extend out over much larger distances from the interface. For example, the data for −2.0 V show eight well-defined ion pair layers (with the last layer at ~8 nm) compared to four layers at ocp (−0.16 V *vs.* Pt). Similarly, there are five ion pair layers shown in Fig. 7b. It should be noted that the force profile for −1.0 V sometimes showed up to seven ion pair layers, but this was not observed consistently enough to be commented upon in detail.

The second important difference at cathodic surface potentials is that, in every instance, the corresponding push-through forces for steps are higher at −1.0 V than for ocp (and likewise higher at −2.0 V than for −1.0 V). In the context of STM findings described below, the increased rupture force of the innermost cation layer from 18 nN to 28 nN for ocp and −1.0 V, respectively, is important as it shows the IL–surface interaction becomes stronger at more cathodic surface potentials. At −2.0 V, the interfacial (innermost) cation layer is so tightly bound that the AFM tip cannot push through it and move into contact with the surface. Note that as the absolute tip–sample separation distance is not known in an AFM experiment it is possible that more than one tightly bound (undetectable) cation layer is present. The first ion layer detected at 0.54 nm in Fig. 7c therefore equates to an FAP^- anion monolayer, with the 'zero' separation corresponding to at least one strongly bound cation monolayer.

Finally, the measured width of the cation monolayer decreases from 0.35 nm at ocp to 0.25 nm at −1.0 V. This indicates that the innermost measurable cation layer adopts a flatter, more compact orientation in response to the higher surface charge, consistent with SFG measurements at the Pt/IL interface.[20] As the AFM tip is not able to probe the adsorbed cation layer at −2.0 V, it is not possible to comment on the precise orientation although a similarly flat arrangement is expected.

All three changes suggest the near surface IL arrangement becomes enhanced when a more negative charge is applied to the Au(111) surface. This indicates that the electric field is inducing structure in the IL close to the interface. In a subsequent paper[50] the effect of a positive surface potential on the IL structure will be also described.

STM measurements

In situ STM measurements were used to evaluate the influence of the IL species on electrode/IL interface. All images were obtained by scanning from the bottom to the top of the image with a slow scan rate of 2 Hz and an image resolution of 512 pixels per line. The approach was done at the ocp (−0.2 V), and then the WE potential was slowly changed during scanning towards more negative electrode potentials. Fig. 8 shows *in situ* STM images of the Au(111) surface under $[Py_{1,4}]FAP$ at different electrode potentials. At the ocp the Au(111) surface is characterized by large flat terraces separated by steps of about 250 pm in height (*cf.* Fig. 8a). Between −0.5 V and −0.7V surface reconstruction is first noted (Fig. 8b) and when the potential is decreased to −1.2 V the Au surface is completely reconstructed, with terraces exhibiting a long-range ("herringbone") superstructure pattern (Fig. 8c). Gold is a face-centered-cubic (fcc) metal that undergoes a reconstruction of the (111) surface; many papers have examined the complex reconstruction of Au(111) in vacuum using STM.[40,51–54] The $(22 \times \sqrt{3})$ reconstruction of the Au(111) surface (unit cell consisting of 23 atoms and known as the Herringbone structure) is easy to recognize with the STM by the presence of stacking fault lines on the surface. The surface layer reduces its energy by formation of stacking structures on the surface, in which the atoms occupy fcc and hexagonal closed-packed (hcp) sites. Since the fcc structure is energetically more favorable than the hcp structure, the width of the hcp stacking is smaller.[55] Similar reconstructions have been noted for Au electrodes in aqueous solutions,[56–60] where the electrode potential applied to the surface may lead to surface reconstruction. Furthermore, the specific adsorption of anions may lift the reconstruction.[59] Fig. 9 shows the $(22 \times \sqrt{3})$ reconstruction of the Au(111) surface in $[Py_{1,4}]FAP$ at −1.2 V. The local structures such as U-connections (neighboring herringbone ridges) and the elbows (a corner made by rotating the herringbone ridge) are clearly identified (Fig. 9a). Such structures are generally observed on

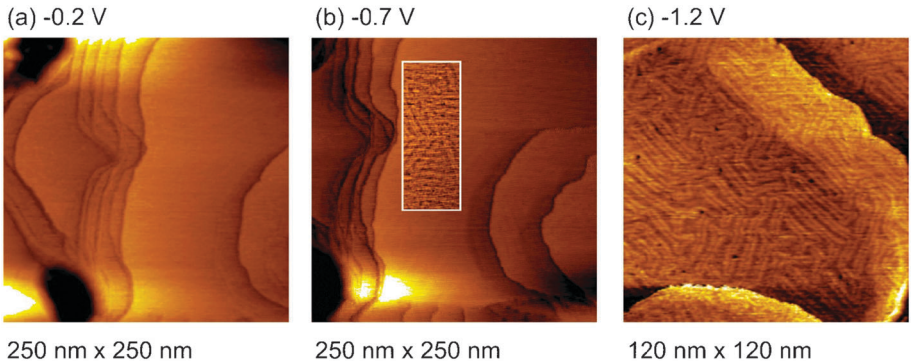

Fig. 8 *In situ* STM images of the Au(111) surface in $[Py_{1,4}]FAP$ at different electrode potentials. In Fig. 8b we have made the evolving structure better visible by a local increasing of contrast.

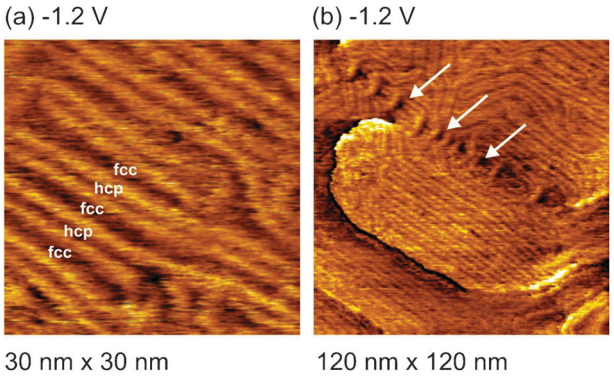

Fig. 9 *In situ* STM images of herringbone structures of the Au(111) surface in $[Py_{1,4}]FAP$ at −1.2 V.

Au(111),[40,52–54] but they have not yet been reported for ionic liquids. With the calibrated STM scanner the distance between the herringbone rims is about 6.0 ± 0.5 nm. This value is a bit lower than the 6.3 nm expected for the $(22 \times \sqrt{3})$ reconstruction. We assume that the adsorbed cation layer (obtained with AFM) might influence the herringbone structure resulting in a slightly different periodicity. Furthermore, the likely multiple contact between the STM tip and the adsorbed cation layer makes an exact evaluation difficult. In Fig. 9b a sequence of loop-shaped structures (marked by arrows) are probed. Such structures seem to be similar to the screw dislocations obtained on the reconstructed Au(111) surface in vacuum.[53] The authors assumed that at this site the STM tip probes the connection of one of the herringbone ridges with another ridge. Interestingly, by further reducing of the electrode potential, the Au(111) surface changes again and at −2.0 V we get the typical flat terraces of Au(111), Fig. 10.

The differences in surface morphology as a function of the potential are attributed to the specific interaction of the IL species with the Au surface. In 2006 it was reported by the Clausthal group that Au(111) in ultra pure $[Py_{1,4}]TFSA$ IL exhibits a herringbone-like reconstruction upon application of a negative electrode potential (−1.6 V).[61] In contrast, when ILs with an imidazolium cation ([EMIm]TFSA) are employed, the Au(111) surface does not show the herringbone structures under the same experimental conditions. With [EMIm]FAP we have also not yet seen the herringbone structure.

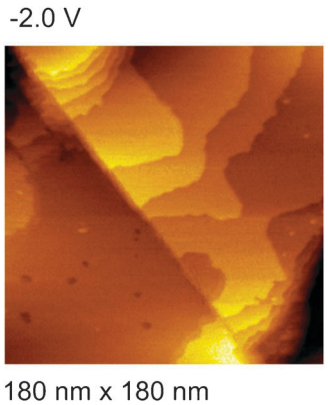

Fig. 10 *In situ* STM image of the Au(111) surface in $[Py_{1,4}]FAP$ at −2.0 V.

The AFM measurements of the Au(111)/$[Py_{1,4}]FAP$ interface reveal that up to 4 layers can be detected at ocp conditions. The typical size of the innermost layer is about 0.35 nm. By decreasing the electrode potential the number of the layers increases and at −2.0 V at least 8 layers can be clearly identified. However, the typical size of the innermost layer decreases by reducing the electrode potential and it is about 0.25 nm at −1.0 V. The cation is expected to be electrostatically adsorbed at negative surface potentials and as the FAP^- anion is large and bulky with a high degree of charge delocalization a weaker surface adsorption for the anion results. These results suggest that the interfacial (innermost) layer also has a templating effect on subsequent layering. Furthermore, preliminary distance tunneling spectroscopy (DTS) measurements show that the work function is dependent on the electrode potential. The tunneling barrier is lowest at the potential regime where the herringbone structure is observed and rises towards more positive and more negative potentials. Since the electrode potential of the tip was constant for all measurements, tunneling spectroscopy probes changes at the Au(111)/$[Py_{1,4}]FAP$ interface. A detailed tunneling spectroscopy study is under progress and will be reported in a future paper. In light of these results, it appears that varying the electrode potential causes not only a reorientation and rearrangements of the IL ions at the interface. It also influences the structure of the interfacial (innermost) layer and causes a reconstruction of the Au surface. Together with the AFM results, we assume that the electrons tunnel between tip and surface through the IL layer closest to the surface. This interpretation is supported by the slightly noisy STM images of the herringbone superstructure. Our results also show that the understanding of the complex interface IL(s)/electrode(s) ideally requires complementary techniques and ILs of the highest possible quality.

Conclusions

In this paper we have presented a combined fundamental *in situ* STM, AFM and EIS study on the structure and dynamics of the interfacial layers between extremely pure $[Py_{1,4}]FAP$ IL and Au(111). *In situ* STM experiments show for the first time that in the cathodic regime the Au(111) surface undergoes a $(22 \times \sqrt{3})$ surface reconstruction in $[Py_{1,4}]FAP$ IL, leading to the "famous" herringbone superstructure. The AFM measurements show that upon applying cathodic electrode potentials the IL becomes more structured in response to the electric field with both number of detectable layers and push-through forces increasing compared to ocp. Tunneling spectroscopy reveals a decrease of the tunneling barrier.

The EIS measurements reveal the existence of three distinct processes at the IL/Au(111) interface taking place on different time scales. The fastest process is characterized by its capacitive low-frequency limiting behavior and is identified with EDL formation. The slowest process detected below 1 Hz exhibits a faradaic behavior in the low-frequency limit (phase angle close to 0°). This process is particularly slow at potentials close around 0 V *versus* Pt RE and becomes faster when the potential is scanned into the cathodic regime. In a narrow potential range between −0.84 V and −1.04 V, a second capacitive

process is detected, which is slower than EDL formation, but faster than the faradaic process. The STM results indicate that the major part of the herringbone reconstruction takes place in this potential range. Therefore, we suggest that the second capacitive process reflects the slow charge flow to the electrode caused by the reconstruction process.

We can conclude that the interface IL/electrode is highly complex. Apart from the dependence of the electrode potential it is likely that these layers are also influenced by added solutes and consequently electrochemical processes in ILs are influenced by several parameters.

Acknowledgements

This work was financially supported by the Deutsche Forschungsgemeinschaft (DFG) within the Priority Program SPP 1191-Ionic Liquids, by the Fonds der Chemischen Industrie (PhD stipend for M. D.), and by an Australian Research Council Discovery Project (DP0986194). The Clausthal group thanks Professor Dieter Kolb (Ulm, Germany) for encouraging us to have a closer look on the herringbone superstructure. The Newcastle group thanks Assoc. Professor Scott Donne for loan of the potentiostat. R.H. thanks the University of Newcastle for a PhD stipend.

References

1 S. Zein El Abedin, E. M. Moustafa, R. Hempelmann, H. Natter and F. Endres, *ChemPhysChem*, 2006, **7**, 1535.
2 P. Eiden, Q. Liu, S. Zein El Abedin, F. Endres and I. Krossing, *Chem.–Eur. J.*, 2009, **15**, 3426.
3 E. M. Moustafa, S. Zein El Abedin, A. Shkurankov, E. Zschippang, A. Bund, A. Y. Saad and F. Endres, *J. Phys. Chem. B*, 2007, **111**, 4693.
4 F. Endres, O. Höfft, N. Borisenko, L. H. Gasparotto, A. Prowald, R. Al Salman, T. Carstens, R. Atkin, A. Bund and S. Zein El Abedin, *Phys. Chem. Chem. Phys.*, 2010, **12**, 1724.
5 M. V. Fedorov and A. A. Kornyshev, *J. Phys. Chem. B*, 2008, **112**, 11868.
6 M. V. Fedorov and A. A. Kornyshev, *Electrochim. Acta*, 2008, **53**, 6835.
7 S. A. Kislenko, I. S. Samoylov and R. H. Amirov, *Phys. Chem. Chem. Phys.*, 2009, **11**, 5584.
8 M. Eigen and E. Wicke, *J. Phys. Chem.*, 1954, **58**, 702.
9 M. S. Kilic, M. Z. Bazant and A. Ajdari, *Phys. Rev. E: Stat., Nonlinear, Soft Matter Phys.*, 2007, **75**, 021502.
10 A. A. Kornyshev, *J. Phys. Chem. B*, 2007, **111**, 5545.
11 R. Hayes, S. Imberti, G. G. Warr and R. Atkin, *Phys. Chem. Chem. Phys.*, 2011, **13**, 3237.
12 R. Atkin and G. G. Warr, *J. Phys. Chem. C*, 2007, **111**, 5162.
13 D. Wakeham, R. Hayes, G. G. Warr and R. Atkin, *J. Phys. Chem. B*, 2009, **113**, 5961.
14 R. Hayes, S. Zein El Abedin and R. Atkin, *J. Phys. Chem. B*, 2009, **113**, 7049.
15 R. Atkin, S. Zein El Abedin, L. H. S. Gasparotto, R. Hayes, N. Borisenko and F. Endres, *J. Phys. Chem. C*, 2009, **113**, 13266.
16 R. Hayes, G. G. Warr and R. Atkin, *Phys. Chem. Chem. Phys.*, 2010, **12**, 1709.
17 M. Mezger, H. Schröder, H. Reichert, S. Schramm, J. S. Okasinski, S. Schröder, V. Honkimäki, M. Deutsch, B. M. Ocko, J. Ralston, M. Rohwerder, M. Stratmann and H. Dosch, *Science*, 2008, **322**, 424.
18 Y. Jeon, J. Sung, W. Bu, D. Vaknin, Y. Ouchi and D. Kim, *J. Phys.Chem. C*, 2008, **112**, 19649.
19 C. S. Santos and S. Baldelli, *J. Phys. Chem. B*, 2009, **113**, 923.
20 S. Baldelli, *Acc. Chem. Res.*, 2008, **41**, 421.
21 M. T. Alam, M. M. Islam, T. Okajima and T. Ohsaka, *J. Phys. Chem. C*, 2007, **111**, 18326.
22 M. T. Alam, M. M. Islam, T. Okajima and T. Ohsaka, *Electrochem. Commun.*, 2007, **9**, 2370.
23 M. T. Alam, M. M. Islam, T. Okajima and T. Ohsaka, *J. Phys. Chem. C*, 2008, **112**, 2601.
24 M. T. Alam, M. M. Islam, T. Okajima and T. Ohsaka, *J. Phys. Chem. C*, 2008, **112**, 16600.
25 M. M. Islam, M. T. Alam and T. Ohsaka, *J. Phys. Chem. C*, 2008, **112**, 16568.
26 V. Lockett, R. Sedev, J. Ralston, M. Horne and T. Rodopoulos, *J. Phys. Chem. C*, 2008, **112**, 7486.
27 F. Silva, C. Gomes, M. Figueiredo, R. Costa, A. Martins and C. M. Pereira, *J. Electroanal. Chem.*, 2008, **622**, 153.
28 M. Gnahm, T. Pajkossy and D. M. Kolb, *Electrochim. Acta*, 2009, **55**, 6212.
29 M. Drüschler, B. Huber, S. Passerini and B. Roling, *J. Phys. Chem. C*, 2010, **114**, 3614.
30 L. Siinor, K. Lust and E. Lust, *Electrochem. Commun.*, 2010, **12**, 1058.
31 L. Siinor, K. Lust and E. Lust, *J. Electrochem. Soc.*, 2010, **157**, F83.
32 J. P. Zheng, P. C. Goonetilleke, C. M. Pettit and D. Roy, *Talanta*, 2010, **81**, 1045.
33 R. T. Gore, T. Bond, W. Zhang, R. W. J. Scott and I. Burgess, *Electrochem. Commun.*, 2010, **12**, 1340.
34 V. Lockett, M. Horne, R. Sedev, T. Rodopoulos and J. Ralston, *Phys. Chem. Chem. Phys.*, 2010, **12**, 12499.
35 N. Hirai, T. Yokogawa and T. Tanaka, *Jpn. J. Appl. Phys.*, 2006, **45**, 2295.
36 Y. Z. Su, Y. C. Fu, J. W. Yan, Z. B. Chen and B. W. Mao, *Angew. Chem., Int. Ed.*, 2009, **48**, 5148.
37 F. Endres, S. Zein El Abedin and N. Borisenko, *Z. Phys. Chem.*, 2006, **220**, 1377.
38 N. Batina, A. S. Dakkouri and D. M. Kolb, *J. Electroanal. Chem.*, 1994, **370**, 87.
39 M. H. Hölzle, Th. Wandlowski and D. M. Kolb, *J. Electroanal. Chem.*, 1995, **394**, 271.
40 J. V. Barth, H. Brune, G. Ertl and R. J. Behm, *Phys. Rev. B: Condens. Matter*, 1990, **42**, 9307.
41 D. Dickertmann, F. D. Koppitz and J. W. Schultze, *Electrochim. Acta*, 1976, **21**, 967.
42 F. C. Anson and J. J. Lingane, *J. Am. Chem. Soc.*, 1957, **79**, 4901.
43 G. A. Snook, A. S. Best, A. G. Pandolfo and A. F. Hollenkamp, *Electrochem. Commun.*, 2006, **8**, 1405.
44 J. L. Hutter and J. Bechhoefer, *Rev. Sci. Instrum.*, 1993, **64**, 1868.
45 E. J. Wanless, T. J. Senden, A. M. Hyde, T. J. Sawkins and G. A. Heath, *Rev. Sci. Instrum.*, 1994, **65**, 1019.
46 *Impedance Spectroscopy. Theory, Experiment, and Applications*, ed. E. Barsoukov and J. R. Macdonald, John Wiley & Sons, Inc., Hoboken, New Jersey, 2nd edn, 2005.
47 M. E. Orazem and B. Tribollet, *Electrochemical Impedance Spectroscopy*, John Wiley & Sons, Inc., Hoboken, New Jersey, 2008.
48 *Broadband Dielectric Spectroscopy*, ed. F. Kremer and A. Schönhals, Springer-Verlag, Berlin, Heidelberg, 2003.
49 A. Triolo, O. Russina, H. J. Bleif and E. DiCola, *J. Phys. Chem. B*, 2007, **111**, 4641.
50 R. Hayes, N. Borisenko, S. Z. El Abedin, F. Endres and R. Atkin, *J. Phys. Chem. C*.
51 Ch. Wöll, S. Chiang, R. J. Wilson and P. H. Lippel, *Phys. Rev. B*, 1989, **39**, 7988.
52 V. Repain, J. M. Berroir, S. Rousset and J. Lecoeur, *Appl. Surf. Sci.*, 2000, **162**, 30.
53 H. Oka and K. Sueoka, *Jpn. J. Appl. Phys.*, 2005, **44**, 5430.
54 Y. Hasegawa and Ph. Avouris, *Science*, 1992, **258**, 1763.
55 S. Narasimhan and D. Vanderbilt, *Phys. Rev. Lett.*, 1992, **62**, 1564.
56 D. M. Kolb, *Prog. Surf. Sci.*, 1996, **51**, 109.
57 J. Schneider and D. M. Kolb, *Surf. Sci.*, 1988, **193**, 579.
58 N. J. Tao and S. M. Lindsay, *Surf. Sci.*, 1992, **274**, L546.
59 D. M. Kolb, *Angew. Chem., Int. Ed.*, 2001, **40**, 1162.
60 D. M. Kolb and J. Schneider, *Electrochim. Acta*, 1986, **31**, 929.
61 N. Borisenko, S. Zein El Abedin and F. Endres, *J. Phys. Chem. B*, 2006, **110**, 6250.
62 M. V. Fedorov, N. Georgi and A. A. Kornyshev, *Electrochem. Commun.*, 2010, **12**, 296.
63 J. Vatamanu, O. Borodin and G. D. Smith, *J. Am. Chem. Soc.*, 2010, **132**, 14825.